Epitaxial growth of (100)-oriented SmN directly on (100)Si substrates

J. F. McNulty,* K. Temst, M. J. Van Bael, A. Vantomme, and E.-M. Anton†

Quantum Solid State Physics, Department of Physics and Astronomy,

KU Leuven, Celestijnenlaan 200D, 3001 Leuven, Belgium

(Dated: November 9, 2021)

We demonstrate growth of epitaxial (100)SmN thin films directly on (100)Si surfaces. By using physical vapor deposition of Sm metal in an N_2 atmosphere we show that careful control of substrate temperature, N_2 pressure, and post annealing steps leads to epitaxial SmN without the formation of samarium silicide impurity phases. While rare-earth silicide formation competes with and is favored over nitride formation at high growth temperatures, we find that low temperature grown SmN seed layers are stable against high temperature annealing, and thus allow for subsequent high temperature growth of SmN with a clear epitaxial relationship to the Si substrate. The relatively low lattice mismatch of SmN with (100)Si, compared to other commonly available substrates, coupled with the low cost and maturity of Si processing technology provide a promising route for further studies of the fundamental properties of SmN and other isostructural members of the rare-earth nitride series. Because SmN is a ferromagnetic semiconductor which also becomes superconducting close to 4 K under sufficient doping, integration with Si technology presents new opportunities for spin-transport devices.

INTRODUCTION

Over the last decade, many of the rare-earth nitrides have been studied as thin films of a few hundred nanometers, including SmN. The interest in these rare-earth nitride thin films stems from their unique electronic and magnetic properties, which have applications in spintronic devices [1–6]. Like a number of other nitrides, SmN is a semiconductor with a direct band gap of 1.27 eV [7], but is also ferromagnetic due to the local moments arising from the $4f$ shell. The electrons in the $4f^5$ configuration of Sm^{3+} produce both spin and orbital magnetic moments each of magnitude as large as ~ 2 μ_B/Sm^{3+}, but which are fixed antiparallel by the $4f$ spin-orbit coupling. The result is that the net ferromagnetic moment is only about 0.035 μ_B, with the orbital moment dominating [8–10]. This unusual situation has been exploited in exchange-coupled magnetic multilayers to produce exchange-springs or twisted magnetizations [11], and magnetoresistance up to 400 % was demonstrated in SmN/AlN/GdN and SmN/GaN/GdN magnetic tunnel junctions [5, 6]. The vanishingly small net magnetization means there is no fringe field in the device structure which can interfere with spin transport, yet a large spin polarization is present. Furthermore, in SmN films and SmN/GdN superlattices grown with carrier concentrations above $\sim 10^{21}$ cm^{-3}, superconductivity has been observed below 4 K [12].

The preparation of well-ordered epitaxial films of rare-earth nitrides still remains a challenge, mostly due to the limited availability of substrates with lattice parameters a_s matching the $a_f \sim 5$ Å cubic rocksalt structure of the rare-earth nitride films, and because of their tendency to react with some of the best matched substrates at elevated temperatures. Epitaxial films are desirable for fundamental studies of magnetic and electronic prop-erties due to the absence of grain boundaries, while they also provide higher quality interfaces and sharper magnetic switching for device applications. SmN, GdN, DyN, ErN, and LuN thin films were initially grown at room temperature by molecular beam epitaxy (MBE) on a variety of substrates including quartz, silica glass, sapphire and Si covered with its natural oxide [8, 13]. Those room temperature grown films were (111)-textured polycrystalline films. GdN films prepared by reactive ion-beam sputtering at high temperatures of 450 °C on Cr or W buffered Si substrates were also used for early studies on polycrystalline GdN [14].

Epitaxial growth of (100)GdN was realized on (100)MgO substrates by MBE, but the large lattice mismatch $(a_f - a_s)/a_s = +18.7\%$ introduced many defects [15]. For SmN, with a bulk material lattice constant of 5.049 Å [16–18], this lattice mismatch would be even more severe at +20%. Later (100)GdN, SmN and EuN were grown epitaxially on (100)-oriented yttria-stabilized zirconia (YSZ) substrates using MBE and plasma-assisted pulsed laser deposition [19–21]. The small YSZ lattice mismatch of -1.5% for SmN seems ideal for epitaxial growth, but it was found that the oxygen in YSZ reacts with the Sm and forms layers of Sm_2O_3 for up to 5 nm before the SmN film begins to form [21]. Similar oxide layers were formed when growing GdN and EuN on YSZ, believed to be a result of the high mobility of oxygen in YSZ at the elevated temperatures needed for epitaxial growth, typically between 600 and 800 °C [19–21].

A different way to achieve epitaxial growth of rare-earth nitrides is to use the hexagonal (0001) surfaces of GaN and AlN templates on (0001)Al_2O_3 or (111)Si substrates. For most growth temperatures (111)-oriented layers are formed on these surfaces, as demonstrated for films of GdN [22–24], EuN [21, 25] and SmN [21, 26, 27]. The lattice mismatches for these rare-earth nitrides with

AlN and GaN is severe with +10 to +15%. Moreover, the six-fold symmetry of the hexagonal (0001) surface leads to two possible orientations of the 3-fold symmetric (111) rare-earth nitride films, causing twin domain formation [22, 24, 26]. Notably, at very high growth temperatures of 800 °C using a NH$_3$ precursor, SmN grows in (100)-orientation on (0001)AlN, forming three rotational variants [26]. In the case of SmN growth on GaN templates, Sm was found to react with GaN at the initial stages of the growth, leaving segregated Ga metal on the SmN surface, with an additional AlN buffer layer needed to overcome this problem [27]. The common (111)-orientation of the films prevents the in-plane magnetization from lying along a high-symmetry direction, and coupled with the formed twin domains causes complications in the analysis of magnetization measurements, making single rotational domain (100)-oriented rare-earth nitride films more desirable.

An ideal substrate candidate is (100)Si, despite having a -7% lattice mismatch with SmN, which is large but much less severe than the +20% for (100)MgO. Epitaxial integration of the rare-earth nitrides on cubic (100)Si substrates is highly desirable because of their ubiquity in semiconductor electronics, mature processing and low cost of Si-wafer technology. Furthermore, the conductivity of Si can be tuned by p- or n-type doping and can be gated for use in devices, in contrast to insulators like MgO. The small spin-orbit coupling of Si is appealing for spin-transport, making integration of Si and semiconducting rare-earth nitrides, acting as spin-injectors/detectors, an interesting possibility [28]. In this vein there has been recent progress in integrating the ferromagnetic semiconductor EuO directly on Si substrates by sophisticated surface preparation [29].

The propensity to form rare-earth silicides instead of the nitrides at elevated substrate temperatures has so far prevented epitaxial growth of the rare-earth nitrides on Si [1]. In this paper we demonstrate epitaxial growth of (100)SmN directly on (100)Si substrates, using a 2-step growth protocol. A SmN seed layer grown at moderate temperatures prevents silicide formation at the higher temperature used for epitaxial growth of the main SmN layer. The high quality of the films is demonstrated via measurements of structural, magnetic and electronic properties. The direct integration of the rare-earth nitrides with Si-technology is a major step towards their use in future electronic and spintronic devices.

EXPERIMENTAL METHODS

(100)Si substrates (p-type, Boron-doped, 10-100 Ω-cm) were first etched in a 2% HF solution for 1 minute before being placed in an ultra-high vacuum system with base pressure of less than 1×10^{-9} Torr. Substrates were outgassed at 850 °C for one hour, using an open backed sample holder with a tungsten filament heater, while the temperature was measured with a thermocouple. Then 50 nm of homoepitaxial Si was grown at a substrate temperature of 650 °C at a deposition rate of 1 nm/min using an e-beam evaporator. *In-situ* scanning tunneling microscopy (STM) confirmed that the Si substrate was clean with atomically flat terraces after these preparation steps.

SmN forms spontaneously in the presence of molecular nitrogen [30], and so Sm metal was evaporated with an effusion cell while the nitrogen gas pressure (6N purity) was controlled to 3×10^{-5} Torr using a leak valve. The SmN layers were grown at a rate of 0.5 nm/min. In a first step, a 4 nm thick SmN seed layer was grown at a substrate temperature of 120 °C, followed by annealing at 500 °C for 20 min with 1×10^{-6} Torr N$_2$. In a second step, 30 or 60 nm thick SmN layers were grown at a substrate temperature of 400 °C, followed by annealing at 400 °C for 30 min without adding N$_2$. *In-situ* reflection high-energy electron diffraction (RHEED) was used to monitor the substrate preparation and post-growth SmN surfaces. To prevent oxidation, all samples were capped at room temperature with 30 nm amorphous Si, deposited at a rate of 1 nm/min from an e-beam evaporator, before removing from the vacuum chambers.

X-ray diffraction (XRD), rocking curves, ϕ-scans and X-ray reflectivity were measured with a Bruker D8 diffractometer using Cu K$_\alpha$ radiation. The reflectivity curves were fitted with GenX [31] to determine film thicknesses. Magnetic measurements were obtained using a Quantum Design MPMS 3 SQUID VSM magnetometer, with the magnetic field applied in-plane of the thin films. Extreme care was taken to minimise any magnetic contamination of the samples for magnetic measurements, avoiding contact with any iron-containing materials including dust, using polymer or ceramic tweezers for sample handling, fresh GE varnish and low background quartz holders for sample mounting [32]. The background signal of the sample holder including varnish was 6×10^{-8} emu for the 25 mT field cooled measurements, near the detection limit of the SQUID. Electrical resistivity and Hall-effect measurements were performed in a Quantum Design Physical Property Measurement System (PPMS), contacts were made with Al wire-bonding in the van der Pauw geometry.

RESULTS AND DISCUSSION

Epitaxial growth protocol

The growth of SmN depends strongly on the quality of the (100)Si surface. This motivated the deposition of 50 nm of homoepitaxial Si, as described in the previous section, to remove the residual natural oxide and bury any surface contaminations [33, 34]. This method avoids
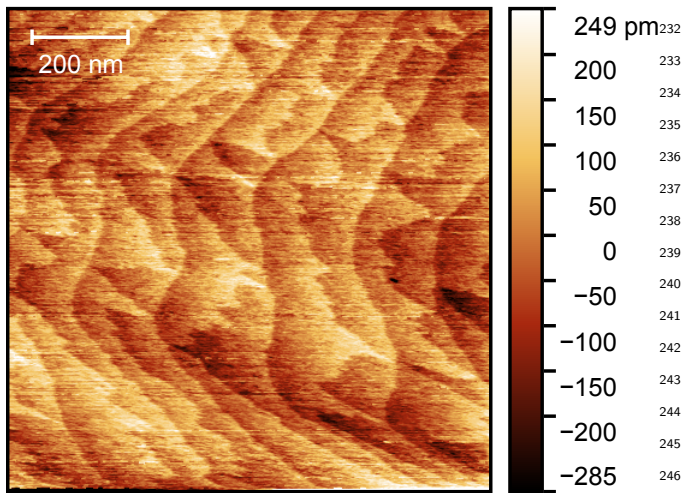
FIG. 1: *In-situ* STM image of the (100)Si substrate after deposition of 50 nm homoepitaxial Si.

the cluster formation, likely from silicon carbide, that was observed by *in-situ* STM after chemically removing the native oxide and annealing at 1000 °C, the maximum temperature available in our system. *In-situ* STM verified that clean terraces with width of 50-100 nm were obtained with our described substrate preparation method, see Fig. 1. The alternating smooth and rough edges of the terraces are typical for Si dimer rows parallel and perpendicular to the step edge, respectively, indicating monoatomic step height. The corresponding RHEED image in Fig. 2 (a) along the $\langle 110 \rangle$ azimuth of (100)Si shows the expected (2×1) surface reconstruction and streaks corresponding to atomically flat terraces. Without the described substrate preparation, the RHEED patterns of SmN contained rings or a superposition of rings and streaks, indicating fully or partially polycrystalline films.

To grow well-ordered epitaxial SmN, high substrate temperatures between 300 and 500 °C are desirable [26, 27], but the silicide reaction is thermodynamically preferred over the nitride formation when growing directly on Si at these high temperatures [1]. We found that an existing SmN seed layer can be annealed at a substantially higher temperature than the substrate temperatures during SmN growth, while still avoiding silicide formation. Moreover, once the Si surface is covered with SmN, subsequent SmN growth is possible in the high temperature range needed for epitaxial growth.

Based on these findings, we developed a 2-step growth protocol, starting with a 3 to 5 nm thin SmN seed layer grown at 120 °C. A higher substrate temperature of 250 °C during growth was found to result in the formation of samarium silicide instead of the nitride during seed layer growth. The nitrogen pressure during seed layer growth, in addition to being necessary for formation of the nitride, also played the crucial role of inhibiting silicide formation. It is known that samarium silicide can form at temperatures just above room temperature without the introduction of nitrogen gas into the chamber [35, 36]. At a substrate temperature of 120 °C, 3×10^{-5} Torr N_2 was sufficient to grow a SmN seed layer, while at 1×10^{-5} Torr the silicide was formed. Subsequent annealing at 500 °C for 20 min in 1×10^{-6} Torr N_2 was performed to improve the quality of the SmN seed layers with thicknesses between 3 and 5 nm. At a higher annealing temperature of 600 °C, 4 nm thick seed layers were found to turn into a silicide, while 5 nm thick layers remained stable. Using seed layers thinner than ~ 3 nm resulted in films with both SmN and silicide phases, as confirmed by XRD. The formation of silicides at either higher temperatures or thinner seed layers is consistent with thin-film dewetting, where the seed layer begins agglomerating into islands, leaving exposed areas of the Si substrate. This process accelerates as the film thickness decreases or temperature increases [37], and thus silicides are favored for seed layers less than ~ 3 nm or temperatures above ~ 120 °C, due to the exposure of the substrate.

In a second step 30 or 60 nm thick SmN was grown on top of the seed layer while holding the substrate at 400 °C. Substrate temperatures of 350 °C yielded partially polycrystalline samples, while at 450 °C we consistently observed silicide formation during the growth of the main SmN layer. Post-growth annealing of the main SmN layer at 400 or 500 °C without N_2 flux improved the film quality as compared to SmN films that were not annealed, as evidenced by a smaller width in the rocking curves. There was no significant difference of the film quality between the two annealing temperatures.

Properties of SmN seed layers after step 1

Fig. 2a presents the RHEED pattern of a (100)Si substrate along the $\langle 110 \rangle$ azimuth after 50 nm of homoepitaxial Si was deposited and just before the SmN seed layer growth. The (2×1) surface reconstruction visible is stable for our growth temperatures and expected for (100)Si substrates after chemical and thermal removal of the native oxide [38]. The RHEED pattern along the $\langle 110 \rangle$ Si azimuth for a 4 nm SmN seed layer after annealing at 500 °C is shown in Fig. 2b, and the pattern along the $\langle 100 \rangle$ Si azimuth is presented in Fig. 3a. The RHEED images show broad streaks with similar lattice spacing as for the (1×1) streaks of the substrate, evidence of the epitaxial alignment of the SmN seed layer with the Si substrate. Intensity modulation along the streaks indicate a stepped surface of multiple atomic heights [39]. The in-plane lattice parameters, derived after calibration with the Si substrate pattern (a_{Si}=5.431 Å, $d_{Si,110}$=3.840 Å), are consistent with a (100)-oriented epitaxial SmN film. The values extracted from the sample in the figures were 3.44 ± 0.14 Å for the electron beam incidence along the

⟨110⟩ azimuth of the Si substrate, and 2.49 ± 0.10 Å along the ⟨100⟩ azimuth. The errors are given for a 4% estimated uncertainty in our lattice parameter determination by RHEED, which stems from the uncertainty in the location of the intensity maxima for both Si and SmN streaks. As compared to the $d_{110} = 3.570$ Å and $d_{200} = 2.525$ Å lattice spacing for bulk SmN with a lattice constant $a = 5.049$ Å [18], the cited d-spacings are 3.7% and 1.4% smaller, respectively. This means any deviation from bulk SmN is within the uncertainty of our measurement. Across our set of samples, the RHEED-determined lattice parameters of the seed layers varied within 4% of the bulk value, again consistent with the measurement uncertainty and not believed to be due to sample preparation. There was no trend towards either tensile or compressive strain within our set of samples, indicating that the seed layer is not systematically strained. A rapid relaxation of epitaxial strain is expected for the large lattice mismatch of -7%, even in a film as thin as 4 nm. In epitaxial (111)GdN grown on (0001)AlN, with $+13\%$ lattice mismatch, the film was relaxed after only 6 monolayers [23]. Strain due to different linear thermal expansion coefficients (CTE) of the SmN film and Si substrate might be present after cooling the samples from the 400 °C growth to room temperature. To our knowledge, CTE for SmN has not been reported, but CTEs for other rare-earth nitrides are available and range from 8×10^{-6} (NdN), 9×10^{-6} (ErN, DyN) to 10×10^{-6} K^{-1} (LaN), with approximately linear lattice expansion in the range from room temperature to 400 °C [40, 41]. Assuming SmN has a similar CTE, the thermal lattice contraction is expected to be between 0.3 to 0.4% after cooling to room temperature, as compared to 0.13% for Si. A thermal strain arising from this mismatch is almost certainly present, but too small to be detected by RHEED. There is no sign of silicide formation or polycrystallinity in the RHEED images of the SmN seed layer.

The XRD pattern of a 5 nm thick SmN seed layer annealed at 600 °C for 30 min is presented in Fig. 4a. For *ex-situ* XRD, this seed layer film was capped with 30 nm amorphous Si before removal from the UHV system. The SmN 200 reflection is clearly visible additionally to the Si 400 substrate peak, despite the small layer thickness. A potential SmN 400 reflection expected around 75° is obscured by the substrate peak. The clearly visible SmN 200 reflection confirms that this layer is indeed SmN with a lattice constant of $a = 5.044 \pm 0.003$ Å , very close to the bulk value. There is no sign of impurity phases or samarium silicide above the detection limit of XRD; this is remarkable given the high annealing temperature of 600 °C.
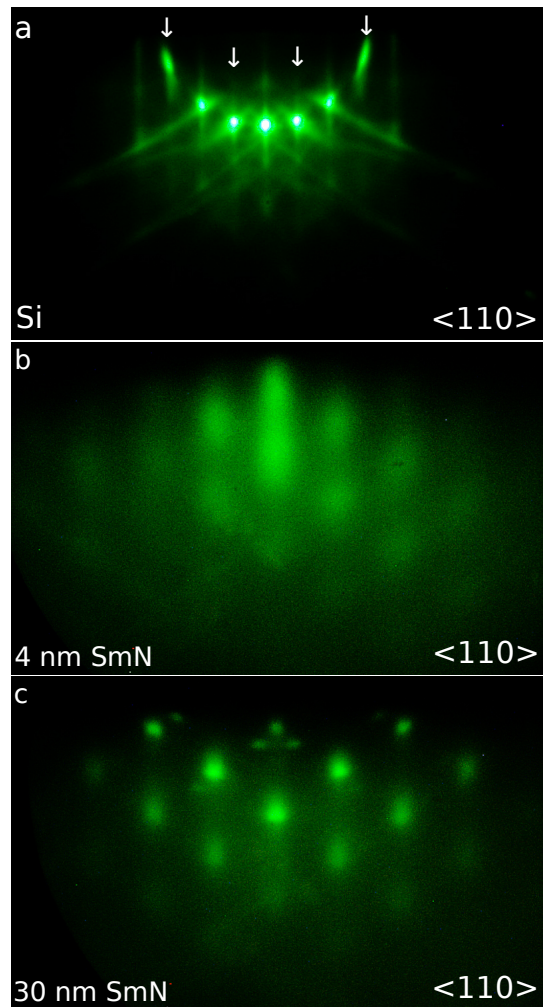
FIG. 2: RHEED patterns along the ⟨110⟩ Si azimuths. a) (100)Si substrate, the arrows mark the additional lines from the (2×1) surface reconstruction, b) 4 nm SmN seed layer and c) 30 nm SmN main layer, each taken at high temperature after their respective annealing step.

Properties of SmN layers after step 2

Figures 2c and 3b show the RHEED patterns along the ⟨110⟩ and ⟨100⟩ Si azimuths of the 30 nm SmN (grown on a 4 nm seed layer) after annealing at 400 °C, respectively. The RHEED shows weak streaks overlapping with a higher intensity spot pattern, with streaks stemming from electron reflection from terraced surfaces and spots resulting from electron transmission through bulk material. This suggests a 3D-island growth mode of the SmN layer, with two distinct patterns along the ⟨110⟩ and ⟨100⟩ azimuths indicating the islands are epitaxially oriented with respect to the substrate. The d-spacings derived from the streak distance were found to be $d_{110} = 3.41 \pm 0.14$ Å and $d_{200} = 2.45 \pm 0.10$ Å . These
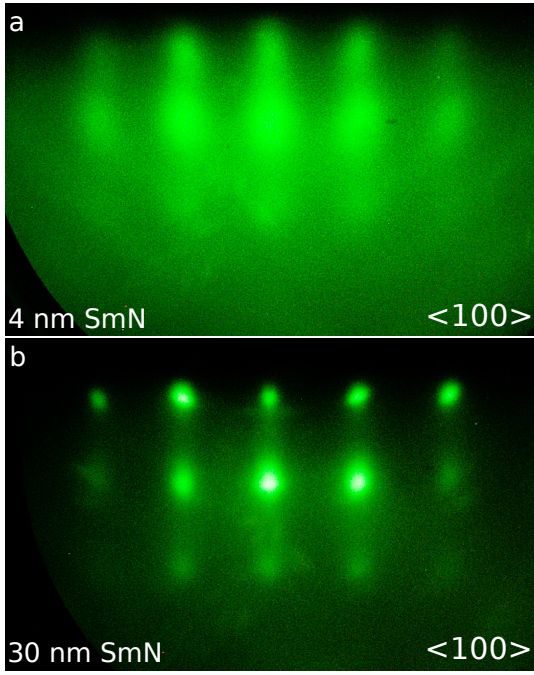
FIG. 3: RHEED patterns along the $\langle 100 \rangle$ Si azimuths. a) 4 nm SmN seed layer and b) 30 nm SmN main layer, each taken at high temperature after their respective annealing step.
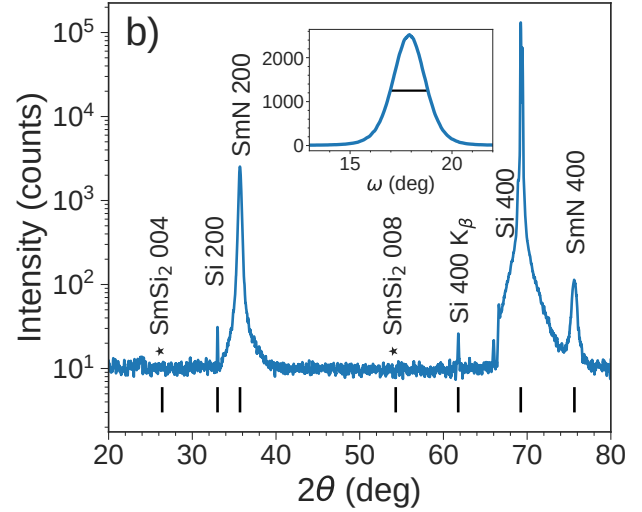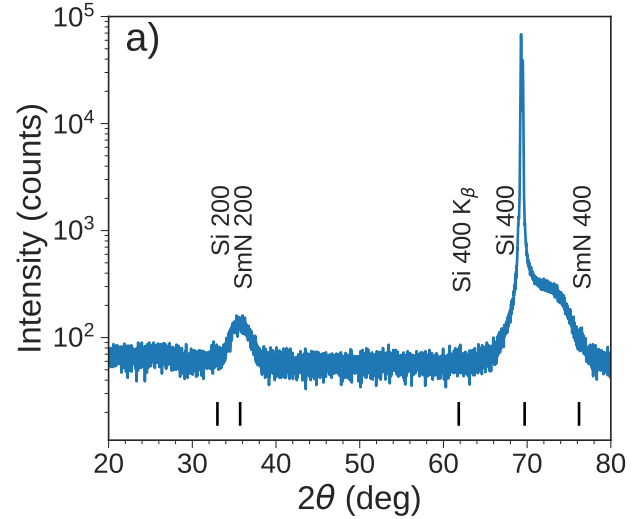

FIG. 4: a) XRD of a 5 nm SmN seed layer after annealing at 600 °C, capped with 30 nm amorphous Si. b) XRD pattern of a 52 nm SmN film. Additionally to the SmN and Si reflections, the positions of the most prominent $SmSi_2$ reflections are marked, proving there is no detectable amount of silicide in this sample. The inset shows the SmN 200 rocking curve with a FWHM of 1.89°.

d-spacings are 4.5 % and 3.1 % smaller compared to the SmN bulk values. As already observed for the seed layer, within our set of samples, in-plane lattice parameters after the growth of the main SmN layer did not indicate a specific strain. They varied about ±5 % around the SmN bulk value, due to the uncertainty of the lattice parameter determination with RHEED discussed in the previous section.

Further evidence of the epitaxial nature and high quality of the SmN films can be found in the XRD pattern in Fig. 4b. All peaks can be identified as either belonging to the epitaxial SmN layer, or the Si substrate. The out-of-plane lattice constant is 5.045 ± 0.005 Å across our set of samples, in agreement with the historic bulk SmN lattice constant of 5.049 Å [18]. For films containing a fraction of samarium silicide, the additional peaks were consistent with a tetragonal $SmSi_2$ phase [42]. The positions of the most prominent 004 and 008 $SmSi_2$ reflections are marked in Fig. 4b and clearly absent in this (100)SmN film. The SmN XRD reflection linewidths provide an estimate of the size of the coherently scattering domains along the growth direction, returning 26 nm and 19 nm for the films of thickness 52 nm and 30 nm, respectively. These values may be taken as a lower limit as microstrain due to defects and vacancies cause additional broadening, so at a minimum the coherently scattering domain size is 50% to 70% of the film thickness, suggesting well ordered films. The SmN 200 rocking curve is shown in the inset of Fig. 4b, with a full width at half maximum (FWHM) equal to 1.89° in this example, showing there is mosaic spread present. FWHMs varied between 1.85° and 3.84° between different samples, and were generally narrower for samples that were annealed after growth.

The in-plane rotational symmetry is investigated in Figure 5, which compares the ϕ-scan of the SmN 111 and Si 111 reflections. Peaks in SmN and the Si substrate occur at the same ϕ angle of rotation about the
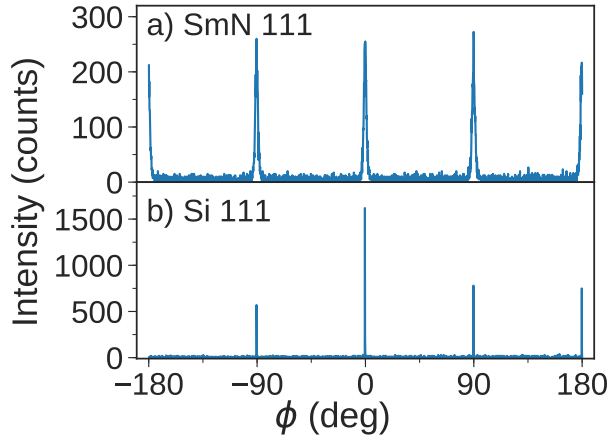
FIG. 5: ϕ-scan of the 111 reflections of a) the SmN layer and b) the Si substrate of the same sample. The 90° spacing of the peaks and the close alignment between SmN and Si peaks are evidence for the cube-on-cube epitaxial relationship.

sample normal, with four-fold symmetry apparent in the 90° spacing. This is consistent with a cube-on-cube epitaxial orientation of SmN and Si.

There are not many studies of epitaxial SmN for comparison of lattice constants. (100)SmN on (100)YSZ had a RHEED in-plane lattice parameter of ∼4.95 Å [21]. Lattice constants for (111)-oriented SmN films grown on (0001)AlN/(111)Si substrates also had a slightly smaller lattice constant than our (100)SmN films with 5.035 Å [26]. Room temperature grown polycrystalline SmN films on the other hand had expanded lattice constants of 5.057 Å to 5.079 Å, with the largest lattice constants found for most nitrogen-rich growths [8, 43]. We have generally observed larger lattice constants for films grown at higher nitrogen pressures or lower growth temperatures. The larger lattice constant films also tend to have smaller carrier concentrations, implying a smaller number of nitrogen vacancies. Epitaxial, high temperature grown films have smaller lattice constants, regardless of the type of substrate used, and larger carrier concentrations, indicating a larger number of nitrogen vacancies. In fact the bulk lattice constant of 5.049 Å measured in Ref. [18] is near the lower end of the lattice constants measured for SmN films, and the bulk material had a measured composition of $SmN_{0.96}$. This suggests stoichiometric SmN may have a larger lattice constant closer to 5.08 Å as found by Shaib *et al.* [43]. As shown below, our epitaxial SmN on Si films have a high carrier concentration, as expected for high-temperature grown films and in line with their relatively small lattice constant.

Magnetic and electrical properties

In Fig. 6a we show the field cooled and zero-field cooled magnetic moment of a 30 nm thick epitaxial (100)SmN film, along with a zero-field cooled measurement of a Si substrate. The diamagnetic Si contribution is large and must be subtracted to obtain the SmN contribution, with the resulting magnetization of the SmN film in μ_B/Sm^{3+} shown in Fig. 6b after correction. The rise in magnetization of the field cooled measurement towards low temperatures is clearly visible, and together with the separation from the zero-field cooled curve just below ∼ 40 K gives a clear indication of ferromagnetism in these samples. A Curie-Weiss susceptibility with constant background was fit below 100 K, yielding a Curie temperature (T_C) of 38±3 K. The small size of the absolute signal in the paramagnetic phase produces a relatively large uncertainty in the constant background, and the temperature-independent van Vleck susceptibility is below the detection limit. Our range of T_Cs between ≈ 33 − 38 K across our samples is typical for SmN, only slightly larger than in an earlier magnetic study on polycrystalline SmN thin films, which found a T_C of 27±3 K [8]. Note that the earlier study on polycrystalline SmN used 300 to 400 nm thick films to achieve a satisfactory signal to noise ratio [8].

Figure 6c shows the temperature dependent resistivity for the same epitaxial SmN film. The positive temperature coefficient of resistance above 50 K is typical of delocalized carriers, indicating a degenerately doped semiconductor or semimetal, with the shape of the curve similar to resistivity data on (111)-epitaxial SmN [44]. The peak in the resistivity curve is located between 18 to 25 K in our (100)SmN films and quite broad. In GdN, the peak in resistivity is linked with the onset of ferromagnetism and is cusp shaped [14, 47, 48]. However, in these (100)SmN films, the temperature at which we observed the peak in resistivity is significantly lower than the magnetic T_Cs found by SQUID measurements. Chan *et al.* [44] did not report magnetic T_C measurements, but found a peak in resistivity at 18 K, also lower than typical SmN T_Cs. These findings suggest different underlying mechanisms may cause the peaks in resistivity in SmN and GdN. This discrepancy is likely related to the nearly compensated spin and orbital $4f$ magnetic moments in SmN which yield a small net magnetization, as well as the fact that the strongly spin-orbit coupled $4f^5$ ground state is not spherically symmetric, in contrast to the spherical $4f^7$ state of GdN with a large 7 μ_B spin moment. Compared to GdN, the non-spherical $4f^5$ state of SmN will have a more complex interaction with the $5d$ states forming the conduction band minimum (via the $4f$-$5d$ exchange), resulting in a different behavior of the resistivity in the main $5d$ conduction channel. A detailed investigation of the interplay between magnetic and transport properties

TABLE I: SmN properties

	a (Å)	T_c (K)	ρ (300 K, $\mu\Omega$-cm)	n (300 K, cm^{-3})	Refs.
(100)SmN/Si	5.04 - 5.05	33 - 38	100 - 200	2×10^{21} - 4.3×10^{21}	this work
(111)SmN/AlN	5.035	—	800 - 1500	1.5×10^{20} - 1×10^{21}	[26, 44]
polycryst. SmN	5.06 - 5.08	27	10^3 - 10^5	2.5×10^{20} - 4×10^{21}	[8, 43, 45]
bulk SmN	5.049	18*	—	—	[18, 46]

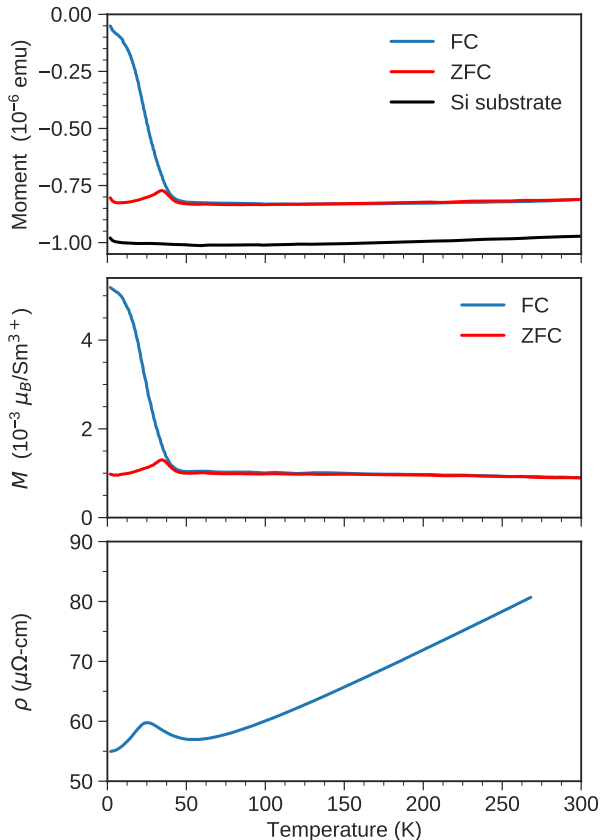* from specific heat measurement, originally labelled antiferromagnetic transition

FIG. 6: a) Field cooled (FC) and zero-field cooled (ZFC) total magnetic moment of a SmN sample which includes a large diamagnetic substrate contribution. Also shown is the total moment of a Si substrate, measured in a magnetic field of 25 mT. b) FC and ZFC magnetization of the SmN film after subtracting the diamagnetic Si contribution shown in a). c) Temperature dependent resistivity measured in zero magnetic field with increasing temperatures.

in SmN will be presented in a future study.

In our epitaxial (100)SmN films room temperature resistivities varied between 100 and 200 $\mu\Omega$-cm. These resistivities are slightly smaller than the 800 to 1500 $\mu\Omega$-cm previously reported for epitaxial (111)-oriented SmN films [44], and much smaller than most room temperature grown polycrystalline SmN films with typical resistivities of the order of 10^3 to 10^5 $\mu\Omega$-cm [12, 45, 49].

Doping levels in the rare-earth nitrides depend on the number of nitrogen vacancies, which is influenced by the nitrogen pressure, substrate temperature and speed of growth. Room temperature grown rare-earth nitride films typically have fewer nitrogen vacancies than high-temperature grown epitaxial films, and thus have smaller electron carrier concentrations and higher resistivities. Calculations have suggested that in GdN, nitrogen vacancies can provide up to three electrons, with two electrons forming a deep level singlet, while a third electron fills the bottom of the $5d$ conduction band [50]. In our epitaxial SmN films, room temperature Hall carrier concentrations were between 2×10^{21} and 4.3×10^{21} cm^{-3} electrons, at the higher end of the literature values which are between 10^{20} to 4×10^{21} cm^{-3} electrons [12, 43–45]. Electron mobilities were between 14 and 35 cm^{2}V^{-1}s^{-1}, in the same range as found for the (111)-epitaxial SmN films [44]. The ranges in measured carrier concentration and mobility reflect the variation between our samples due to slightly different growth conditions, as discussed in the previous section. There is no sign of superconductivity in these (100)-oriented epitaxial films down to 2 K, despite having a similar resistivity and carrier concentration as compared to the (111)-epitaxial films in which superconductivity was discovered [12], suggesting either an influence of the growth orientation or thermal expansion induced strain on the development of the superconducting phase, or a superconducting T_C below 2 K. A summary of the SmN properties of this and other work is presented in Table I.

CONCLUSION

We developed a 2-step growth protocol that allows direct epitaxial integration of (100)SmN with (100)Si, avoiding the commonly occurring formation of rare-earth silicides without the need of a buffer layer of a different composition. A thin SmN seed layer grown at 120 °C was found to be stable during subsequent annealing at 500 °C, and acted both as buffer and epitaxial seed layer for the 400 °C grown main SmN layer. RHEED and XRD confirm the cube-on-cube epitaxial growth of SmN in the (100)-orientation and the absence of impurity phases. Magnetic and electrical measurements confirm that the

epitaxial SmN films are ferromagnets below ~35 K and semimetals or semiconductors heavily doped with electrons. The epitaxial growth of SmN on Si has potential use in spintronic devices and opens up pathways to explore spin injection from a semiconductor into Si. This work could also guide future epitaxial growth of other rare-earth nitrides on Si, allowing tailoring of the magnetic properties and lattice mismatches for both fundamental and applied studies.

ACKNOWLEDGEMENTS

---

* Current affiliation: School of Chemical and Physical Sciences, Victoria University of Wellington, PO Box 600, Wellington 6140, New Zealand

† Author to whom correspondence should be addressed: eva.anton@vuw.ac.nz; Current affiliation: School of Chemical and Physical Sciences, Victoria University of Wellington, PO Box 600, Wellington 6140, New Zealand

[1] F. Natali, B. J. Ruck, N. O. V. Plank, H. J. Trodahl, S. Granville, C. Meyer, and W. R. L. Lambrecht, Prog. Mater. Sci. **58**, 1316 (2013).

[2] K. Senapati, M. G. Blamire, and Z. H. Barber, Nat. Mater. **10**, 849 (2011).

[3] Y. Zhu, A. Pal, M. G. Blamire, and Z. H. Barber, Nat. Mater. **16**, 195 (2017).

[4] P. K. Muduli, A. Pal, and M. G. Blamire, Phys. Rev. B **89**, 094414 (2014).

[5] H. Warring, H. J. Trodahl, N. O. V. Plank, F. Natali, S. Granville, and B. J. Ruck, Phys. Rev. Applied **6**, 044002 (2016).

[6] J. D. Miller, F. H. Ullstad, H. J. Trodahl, B. J. Ruck, and F. Natali, Nanotechnology **31**, 235202 (2020).

[7] W. F. Holmes-Hewett, R. G. Buckley, B. J. Ruck, F. Natali, and H. J. Trodahl, Phys. Rev. B **99**, 205131 (2019).

[8] C. Meyer, B. J. Ruck, J. Zhong, S. Granville, A. R. H. Preston, G. V. M. Williams, and H. J. Trodahl, Phys. Rev. B **78**, 174406 (2008).

[9] E.-M. Anton, B. J. Ruck, C. Meyer, F. Natali, H. Warring, F. Wilhelm, A. Rogalev, V. N. Antonov, and H. J. Trodahl, Phys. Rev. B **87**, 134414 (2013).

[10] J. F. McNulty, B. J. Ruck, and H. J. Trodahl, Phys. Rev. B **93**, 054413 (2016).

[11] J. F. McNulty, E.-M. Anton, B. J. Ruck, F. Natali, H. Warring, F. Wilhelm, A. Rogalev, M. M. Soares, N. B. Brookes, and H. J. Trodahl, Phys. Rev. B **91**, 174426 (2015).

[12] E.-M. Anton, S. Granville, A. Engel, S. V. Chong, M. Governale, U. Zülicke, A. G. Moghaddam, H. J. Trodahl, F. Natali, S. Vézian, and B. J. Ruck, Phys. Rev. B **94**, 024106 (2016).

[13] S. Granville, C. Meyer, A. R. H. Preston, B. M. Ludbrook, B. J. Ruck, H. J. Trodahl, T. R. Paudel, and W. R. L. Lambrecht, Phys. Rev. B **79**, 054301 (2009).

[14] F. Leuenberger, A. Parge, W. Felsch, K. Fauth, and M. Hessler, Phys. Rev. B **72**, 014427 (2005).

[15] J. W. Gerlach, J. Mennig, and B. Rauschenbach, Appl. Phys. Lett. **90**, 061919 (2007).

[16] G. Busch, P. Junod, F. Levy, A. Menth, and O. Vogt, Phys. Lett. **14**, 264 (1965).

[17] F. Hulliger, *Handbook on the Physics and Chemistry of Rare Earths*, edited by J. K.A. Gschneidner and L. Eyring, Vol. 4 (North-Holland, New York, 1979) pp. 153–236.

[18] R. Moon and W. Koehler, J. Magn. Magn. Mater. **14**, 265 (1979).

[19] B. M. Ludbrook, I. L. Farrell, M. Kuebel, B. J. Ruck, A. R. H. Preston, H. J. Trodahl, L. Ranno, R. J. Reeves, and S. M. Durbin, J. Appl. Phys. **106**, 063910 (2009).

[20] J. H. Richter, B. J. Ruck, M. Simpson, F. Natali, N. O. V. Plank, M. Azeem, H. J. Trodahl, A. R. H. Preston, B. Chen, J. McNulty, K. E. Smith, A. Tadich, B. Cowie, A. Svane, M. van Schilfgaarde, and W. R. L. Lambrecht, Phys. Rev. B **84**, 235120 (2011).

[21] F. Natali, B. Ludbrook, J. Galipaud, N. Plank, S. Granville, A. Preston, B. D. Le, J. Richter, I. Farrell, R. Reeves, S. Durbin, H. J. Trodahl, and B. J. Ruck, Phys. Status Solidi C **9**, 605 (2012).

[22] M. Scarpulla, C. Gallinat, S. Mack, J. Speck, and A. Gossard, J. Cryst. Growth **311**, 1239 (2009).

[23] F. Natali, N. O. V. Plank, J. Galipaud, B. J. Ruck, H. J. Trodahl, F. Semond, S. Sorieul, and L. Hirsch, J. Cryst. Growth **312**, 3583 (2010).

[24] F. Natali, S. Vézian, S. Granville, B. Damilano, H. J. Trodahl, E.-M. Anton, H. Warring, F. Semond, Y. Cordier, S. V. Chong, and B. J. Ruck, J. Cryst. Growth **404**, 146 (2014).

[25] B. J. Ruck, H. J. Trodahl, J. H. Richter, J. C. Cezar, F. Wilhelm, A. Rogalev, V. N. Antonov, B. D. Le, and C. Meyer, Phys. Rev. B **83**, 174404 (2011).

[26] J. R. Chan, S. Vézian, H. J. Trodahl, M. A. Khalfioui, B. Damilano, and F. Natali, Cryst. Growth Des. **16**, 6454 (2016).

[27] S. Vézian, B. Damilano, F. Natali, M. A. Khalfioui, and J. Massies, J. Cryst. Growth **450**, 22 (2016).

[28] I. Appelbaum, B. Huang, and D. J. Monsma, Nature **447**, 295 (2007).

[29] D. V. Averyanov, Y. G. Sadofyev, A. M. Tokmachev, A. E. Primenko, I. A. Likhachev, and V. G. Storchak, ACS Appl. Mater. Interfaces **7**, 6146 (2015).

[30] J. R. Chan, S. G. Lambie, H. J. Trodahl, D. Lefebvre, M. Le Ster, A. Shaib, F. Ullstad, S. A. Brown, B. J. Ruck, A. L. Garden, and F. Natali, Phys. Rev. Materials **4**, 115003 (2020).

[31] M. Björck and G. Andersson, J. Appl. Crystallogr. **40**, 1174 (2007).

[32] L. M. C. Pereira, J. P. Araújo, M. J. Van Bael, K. Temst, and A. Vantomme, J. Phys. D: Appl. Phys. **44**, 215001 (2011).

[33] K. Kugimiya, Y. Hirofuji, and N. Matsuo, Jpn. J. Appl. Phys **24**, 564 (1985).

[34] J. P. Becker, R. G. Long, and J. E. Mahan, J. Vac. Sci. Technol. A **12**, 174 (1994).

[35] P. Godowski, F. Ørskov, M. Christiansen, and J. Onsgaard, Thin Solid Films **205**, 35 (1991).

[36] N. G. Gheorghe, G. A. Lungu, M. A. Husanu, R. M. Costescu, D. Macovei, and C. M. Teodorescu, Appl. Surf. Sci. **267**, 106 (2013).

[37] C. V. Thompson, Annu. Rev. Mater. Res. **42**, 399 (2012).

[38] D. Ali and C. J. K. Richardson, J. Vac. Sci. Technol. A **30**, 061405 (2012).

[39] S. Hasegawa, "Characterization of materials," (John Wiley & Sons, Inc., 2012) Chap. Reflection High-Energy Electron Diffraction, pp. 1925–1938, 2nd ed.

[40] G. L. Olcese, J. Phys. F: Metal Phys. **9**, 569 (1979).

[41] M. Takano, S. Tagami, K. Minato, T. Kozaki, and S. Sato, J. Alloys Compd. **439**, 215 (2007).

[42] F. Natali, N. O. V. Plank, B. M. Ludbrook, J. Richter, T. Minnee, B. J. Ruck, H. J. Trodahl, J. V. Kennedy, and L. Hirsch, Jpn. J. Appl. Phys. **49**, 025505 (2010).

[43] A. Shaib, W. F. Holmes-Hewett, J. Chan, P. P. Murmu, B. J. Ruck, H. J. Trodahl, and F. Natali, AIP Advances **11**, 015125 (2021).

[44] J. R. Chan, M. A. Khalfioui, S. Vézian, H. J. Trodahl, B. Damilano, and F. Natali, MRS Advances **2**, 165171 (2017).

[45] W. F. Holmes-Hewett, F. H. Ullstad, B. J. Ruck, F. Natali, and H. J. Trodahl, Phys. Rev. B **98**, 235201 (2018).

[46] W. Stutius, Physik der kondensierten Materie **10**, 152 (1969).

[47] F. Natali, B. J. Ruck, H. J. Trodahl, B. D. Le, S. Vézian, B. Damilano, Y. Cordier, F. Semond, and C. Meyer, Phys. Rev. B **87**, 035202 (2013).

[48] T. Maity, H. J. Trodahl, S. Granville, S. Vzian, F. Natali, and B. J. Ruck, J. Appl. Phys. **128**, 213901 (2020).

[49] A. R. H. Preston, S. Granville, D. H. Housden, B. Ludbrook, B. J. Ruck, H. J. Trodahl, A. Bittar, G. V. M. Williams, J. E. Downes, A. DeMasi, Y. Zhang, K. E. Smith, and W. R. L. Lambrecht, Phys. Rev. B **76**, 245120 (2007).

[50] A. Punya, T. Cheiwchanchamnangij, A. Thiess, and W. R. Lambrecht, MRS Online Proceedings Library (OPL) **1290** (2011).